Dalton Transactions

Accepted Manuscript

ROYAL SOCIETY OF CHEMISTRY

www.rsc.org/dalton

Dalton Transactions

RSC Publishing

ARTICLE

Hierarchical heterostructures based on prickly Ni nanowires/Cu_2O nanoparticles with enhanced photocatalytic activity

Cite this: DOI: 10.1039/x0xx00000x

Received 00th March 2015,
Accepted 00th March 2015

DOI: 10.1039/x0xx00000x

www.rsc.org/

Xiaolin Li, Yujie Ma, Zhi Yang*, Shusheng Xu, Liangming Wei, Da Huang, Tao Wang, Nantao Hu, Yafei Zhang*

Metal-semiconductor-based photocatalysts show high efficiencies and catalytic activities in photocatalysis process. Herein, the magnetic and one-dimensional Ni-Cu_2O heteronanowires have been fabricated via *in situ* reduction of pre-adsorbed Cu^{2+} on the surface of prickly Ni nanowires in ethanol solution for photocatalysis application. The resultant Ni-Cu_2O heteronanowires show higher photocatalytic ability than pure Cu_2O nanoparticles in degradation of methyl orange. The enhancement of photocatalytic efficiency can be ascribed to the unique one-dimensional nanostructure and electron sink effect of Ni nanowires in the heterostructure. It is believed that the low-cost metal Ni is an alternative candidate for substituting the costly metal (Au, Ag and Pt) to improve the photocatalytic ability of semiconductor-based photocatalysts.

1 Introduction

Metal oxide semiconductors, such as TiO_2, ZnO and Cu_2O, have aroused great scientific and engineering interest in photocatalytic fields to solve energy and environment problems.[1-8] Although the metal oxide semiconductors is used extensively in photodegradation of pollutants, the fast recombination of the photogenerated electrons (e^-) and holes (h^+) limits their photocatalytic efficiency. To solve this problem, various strategies have been carried out to design and fabricate highly efficient and active photocatalysts,[9-13] which can be classified into two main categories: (i) semiconductor composites with p–n junction heterostructures[14-20] and (ii) metal-semiconductor composites with Schottky barrier heterostructures.[21-28] Both of them can improve the charge separation at the interfaces and/or enhance light absorption, thus significantly increasing the photocatalytic and light-harvesting efficiencies. Especially for the latter metal/semiconductor photocatalytic system (metal = Ag, Au, Cu and Pt), it can be obtained more directly and simply and retard the recombination rate by transferring e^- to the metal, while the holes can remain in the valence band (VB) of semiconductor.[29-32]

In addition to defer the recombination, semiconductor with narrow-band gap can also facilitate the photocatalytic process by enhancing the absorption of light harvesting. Cuprous oxide is one such an environmentally benign p-type direct semiconductor with a narrow band gap of 2.17 eV which avails the absorption of a large part of visible light and has been widely investigated due to its unique visible-driven photocatalytic properties, low cost and abundance of its raw materials.[30,33-39] Various metal–Cu_2O heteroarchitectures have been designed to improve the photocatalytic activity, such as Au/Ag@Cu_2O core–shell nanowires and nanosphreres, and Au@Cu_2O octahedra and nanocubes.[25,27,28,40,41] It is expected that the surface plasmon resonance of noble metal nanoparticles can enhance absorption of incident photons, which will improve the photocatalytic efficiency of the semiconductors.[25,28] Recently, the transition metal copper was also employed to prepare

Cu-Cu_2O photocatalyst which showed excellent photocatalytic ability towards the decomposition of dye.[31,42-44] In addition, nickel nanoparticles have shown important applications in catalysts due to its magnetic properties and multifunctiomal use.[45,46,47] However, to the best of our knowledge, there is still no report on the synthesis of highly efficient metal-Cu_2O photocatalysts with other low-cost metal, except Cu.

In this contribution, this is the first time to incorporate metal Ni nanowires (NWs) into Cu_2O nanoparticles (NPs) to prepare magnetic quasi one-dimensional (1D) Ni-Cu_2O heteronanowires (HNWs) with enhanced photocatalytic ability. The results demonstrated that the photocatalytic activity of Ni-Cu_2O HNWs is superior to that of pure Cu_2O NPs on the photodegradation of methyl orange (MO). This is an appealing and potential photocatalytic system, because (i) the unique 1D geometry can provide fast and long-distance electron transfer, superior electron conductivity and mobility, and light-harvesting efficiency; (ii) the photocatalysts are easily to be recycled due to the magnetic Ni NWs in the composites, and thus avoid the secondary pollution; (iii) the preparation process is low-cost and suitable for mass production.

2 Experimental

2.1 Chemicals

All of the chemicals were analytical grade and used directly without further purification. Copper (II) nitrate 3-hydrate ($Cu(NO_3)_2 \cdot 3H_2O$), hydrazine solution ($N_2H_4 \cdot H_2O$, 85 wt% in water), ethylene glycol, methanol, ethanol, propanol, acetone, sodium hydroxide (NaOH), nickel (II) chloride hexahydrate ($NiCl_2 \cdot 6H_2O$), methyl orange (MO), rhodamine B (RhB), and orange G (OG) were all purchased from Sinopharm Chemical Reagent Co., Ltd (Shanghai, China). Polyvinylpyrrolidone (PVP, Mw = 55000) was purchased from Sigma-Aldrich. Deionized (DI) water with a resistivity of 18.1 MΩ•cm was used for all experiments.

2.2 Synthesis of prickly nickel nanowires (Ni NWs)

The Ni NWs were prepared by a modified process.[48,49] Typically, 0.5 g of $NiCl_2 \cdot 6H_2O$ was dissolved in 100 mL of ethylene glycol containing 4 g of PVP, stirring until the solution became homogeneous. Separately, 2 g of NaOH was dissolved in 100 mL of ethylene glycol. Then, the two solutions were mixed, followed by the addition of 20 mL of $N_2H_4 \cdot H_2O$ (85 wt% in water), after which the colour of solution immediately changed from green to blue. Subsequently, the mixture solution was transferred to a water bath and heated from 25 to 80 °C under magnetic field. After heating at 80 °C for 1 h, the obtained grey-black fluffy Ni NWs were separated from the solution using a magnet and washed several times with water, acetone and absolute ethanol, respectively, and then the products were dispersed in 100 mL of ethanol and finally stored in a refrigerator at 4 °C for further investigation.

2.3 Preparation of Ni-Cu_2O HNWs

Typically, 5 mL of Ni NWs ethanol solution was added dropwise into 50 mL of 0.05 M $Cu(NO_3)_2$ ethanol solution (transparent blue) under sonication for 15 min. Then, the mixture solution was stirred by mechanical stirring for 30 min. After successful surface decoration by Cu^{2+}, 100 μL of diluted $N_2H_4 \cdot H_2O$ (35.4 wt% in water) was quickly injected into the solution under continuously stirring for another 30 min, immediately forming plenty of flocculation. The resultant samples were centrifuged for 5 min and washed with cold water for the first time, after which the suspension became yellow indicating the formation of Cu_2O NPs. Then, poured out the excess Cu_2O suspension and washed the precipitation by using ethanol for several times until the suspension became clear. The resultant nanoparticles were dried in a vacuum oven at 30 °C overnight, and the powder was sealed and stored at room temperature.

2.4 Synthesis of pure Cu_2O NPs

The pure Cu_2O NPs were synthesized using the above similar procedure of Ni-Cu_2O HNWs without adding Ni NWs solution.

2.5 Photocatalytic activity measurement

The photocatalytic activity of samples was evaluated by the degradation of MO in an aqueous solution under light irradiation. To ensure the weight of pure Cu_2O NPs is the same as that in Ni-Cu_2O HNWs, 20 mg of Ni-Cu_2O HNWs, Ni NWs, and 2.5 mg of pure Cu_2O NPs were completely dispersed into 100 mL of MO aqueous solution (20 mg/mL), respectively. The value of 2.5mg pure Cu_2O is calculated according to results of ICP (As shown in Table S1). This design can convectively manifest the synergistic effect between Cu_2O NPs and Ni NWs to improve the photocatalytic efficiency. Before irradiation, each solution was stirred in the dark for 30 min to ensure adsorption-desorption equilibrium between the catalysts and MO. The tests were carried out by exposing the suspension to a

300W Xe lamp with UV cutoff filter (λ< 420 nm). After given time intervals, 4 mL of the suspension was taken out and then centrifuged to remove the photocatalysts for UV-vis absorption measurements, and the characteristic absorption of MO at 464 nm was used to evaluate its photocatalytic degradation behaviour. The percentage of degradability is calculated by $(C_0 - C)/C_0$, where C is the absorption of MO solution at each irradiation time interval, and C_0 is the absorption of the initial concentration when the adsorption-desorption equilibrium is achieved.

2.6 Measurement of electrochemical impedance spectroscopy (EIS)

EIS measurements were performed with an electrochemical workstation (CHI760E, Chenhua, Shanghai, China) in a frequency range from 10 mHz to 100 kHz and an AC amplitude of 5 mV at room temperature. Typically, the Ni-Cu_2O or Cu_2O membrane was obtained by suction-filtered, then dried overnight at 30 °C and pressed at 10 MPa for 5 min. For convenience of followed characterization, all membranes were cut into 0.5 × 0.5 cm^2. A Pt sheet and Ag/AgCl electrode were used as counter electrodeand reference electrode, respectively. Na_2SO_4 (0.01 M) aqueous solution was employed as electrolyte.

2.7 Characterization

The morphologies of the samples were observed by transmission electron microscopy (TEM, JEOL 2100, Japan) and field emission scanning electron microscopy (FE-SEM, Carl Zeiss Ultra Plus, Germany) equipped with energy-dispersive X-ray (EDX) spectrum (Oxford Instruments INCA Penta FET×3, Model:7426). The ultraviolet-visible-near infrared (UV-Vis-NIR) absorption spectra were recorded by a UV-Vis-NIR spectrophotometer (Lambda 950, Perkin-Elmer, USA). Powder X-ray diffraction (XRD) measurements were obtained with a RIGAKU diffractometer equipped with Cu Kα X-ray radiation, operated at 40 kV and 20 mA, and made in Japan. The XRD patterns were recorded from 20° to 100° with a scanning rate of 2°/min. The content of Cu in composite was measured by Inductively Coupled Plasma (ICP, Agilent 7500a, USA). Magnetic hysteresis loop was measured by vibrating sample magnetometer at 300 K (VSM, PPMS-9T (EC-II), USA). The photoluminescence (PL) spectra were performed through a fluorescent spectrophotometer (F-4600, Hitachi, Japan). Brunauer–Emmett–Teller (BET) nitrogen_adsorption–desorption was measured using a V-sorbsystem (ASAP, 2020, USA).

3 Results and discussion

Schematic illustration of the possible formation process is described in Fig. 1. In this process, ethanol was used as solvent to avoid the reduction of Cu^{2+} by Ni NWs due to the quite different standard reduction potential ($\varphi^{\Theta}_{Ni/Ni^{2+}} = -0.25$ V, $\varphi^{\Theta}_{Cu/Cu^{2+}} = +0.34$ V). The mild reducing agent hydrazine with low concentration provides alkaline environment to form $Cu(OH)_2$ flocculation in ethanol. After the first centrifugation, there are still plenty of $N_2H_4{\cdot}H_2O$ molecule absorb on the surface of $Cu(OH)_2$. When aqueous environments is provided, Cu_2O nuclei are formed through the reduction of $Cu(OH)_2$ by $N_2H_4{\cdot}H_2O$. Actually, it is observed that there were many bubbles in aqueous solution when the suspension became yellow. Above all, the possible chemical reactions are depicted in eqn (1-3). The cold water provides low temperatures which can prevent the further reduction of Cu_2O to Cu by $N_2H_4{\cdot}H_2O$.[41,50] The thorns of Ni NWs are expected to be the nucleation site for Cu_2O nanospheres.[35,37]

$$N_2H_4{\cdot}H_2O \xleftrightarrow{C_2H_5OH} N_2H_5^+ + OH^- \quad (1)$$

$$Cu^{2+} + 2OH^- \xrightarrow{C_2H_5OH} Cu(OH)_2 \quad (2)$$

$$4Cu(OH)_2 + N_2H_4 \xrightarrow{H_2O} 2Cu_2O + N_2 + 6H_2O \quad (3)$$

The morphologies of the as-prepared Ni NWs and Ni-Cu_2O HNWs were analyzed by FE-SEM. Typical SEM images (Fig. 2a-c) show that the 1D Ni NWs are of a sharp slender spiny surface. The magnified SEM image in Fig. 2c represents a well-defined Ni NWs with distinct thorns, of which the length ranges from about 20 nm to 230 nm. Fig. 2d-f reveals that Cu_2O NPs with rough surface are densely grown on the entire surface of Ni NWs. The size distribution in Fig. S1 indicates that the average size of Cu_2O NPs in heteronanowires is 92 nm. From Fig. 2f, it is found that some large thorns are exposed vertically to outside of the surface, while small ones are all coated densely by Cu_2O NPs, indicating that Cu_2O NPs more easily form and grow on the thorns with small size.

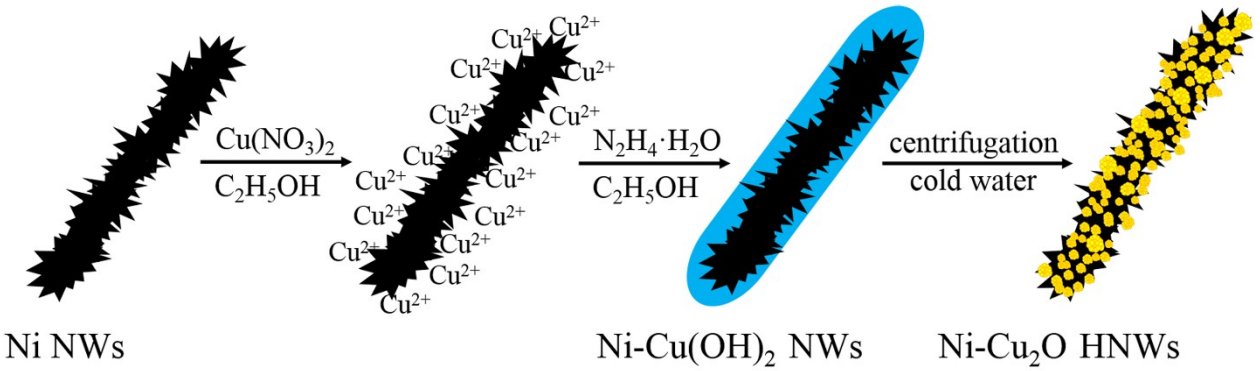

Fig. 1 Schematic illustrations of a typical formation process for 1D Ni-Cu_2O HNWs.

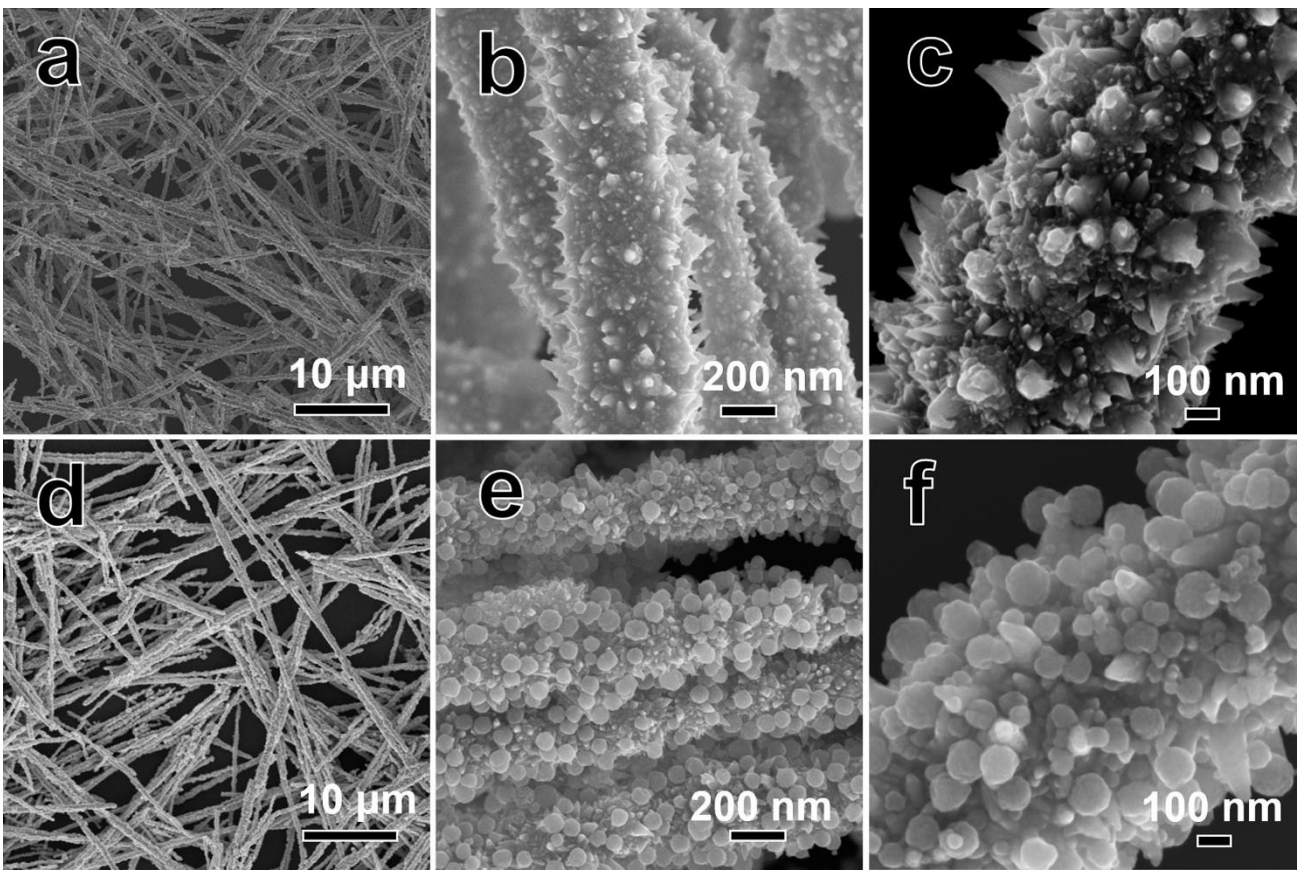

Fig. 2 SEM images of (a-c) Ni NWs and (d-f) Ni-Cu_2O HNWs.

The Ni-Cu_2O HNWs not only keep the 1D nanowire structure, but also inherit magnetism of Ni NWs. The magnetic hysteresis loop in Fig. 3 combined with the expanded low-field hysteresis curve (insert in Fig. 3) measured at 300 K displays that the saturation magnetization (Ms), remnant magnetism (Mr), and the coercivity (Hc) for Ni-Cu_2O HNWs are 43.25 emu/g, 10.22 emu/g, and 230.36 Oe, respectively. The photo in Fig. 3 visually confirms that Ni-Cu_2O HNWs can be separated from a solution by an external magnetic field, which is beneficial for the recycle and can avoid the secondary pollution.

The distribution of elements in Ni-Cu_2O HNWs is shown in Fig. 4b and c. The green, red and blue colours represent the distribution of nickel, copper and oxygen elements, respectively,

which is consistent with the SEM images in Fig. 4a and confirms the effective incorporation of Cu_2O NPs with Ni NWs. The EDX spectrum provided in Fig. S2 further demonstrates that Ni-Cu_2O HNWs is mainly composed of Ni, Cu and O. According to the ICP results of Cu element in Ni-Cu_2O HNWs (Table S1), the average content of Cu_2O is 12.4 wt% in the composites.

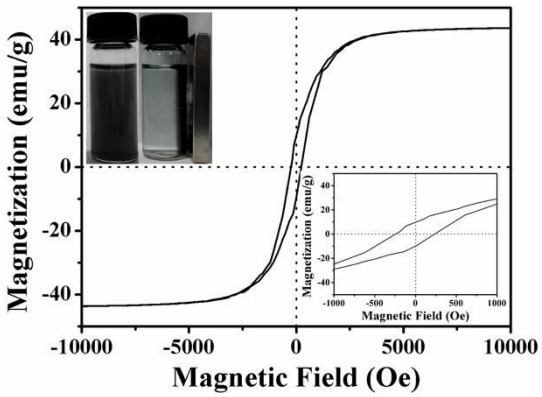

Fig. 3 Magnetic hysteresis loop of Ni-Cu_2O HNWs measured at 300 K. The insert in the bottom right is an expanded low field hysteresis curve, and the inset in the top left is the photo of Ni-Cu_2O HNWs before (left) and after (right) separation by an external magnetic field.

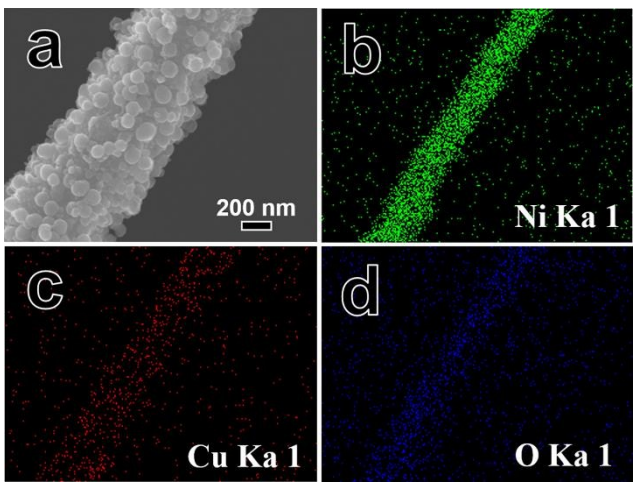

Fig. 4 (a) SEM image of Ni-Cu_2O HNWs, and elemental mapping of (b) Ni, (c) Cu, and (d) O element.

The detailed microstructure of Ni-Cu_2O HNWs was further studied by TEM and XRD. Fig. 5b and c show the high resolution TEM images taken from the red arrows region in Fig. 5a, which reveals that both Ni NWs (solid arrow) and Cu_2O NPs (dotted arrow) grow along [111] direction with the lattice fringes of 0.204, 0.248 and 0.214 nm, corresponding to Ni (111), Cu_2O (111) and (200), respectively. The corresponding XRD pattern is shown in Fig. 5d, in which every peak can be indexed to pure cubic-phase Ni (JCPDS 4−850) and Cu_2O (JCPDS 5−667) with lattice constants of 3.52 and 4.27 Å, respectively, demonstrating the formation of Ni-Cu_2O HNWs. There are no other impurity peaks attributed to Cu or CuO, which indicates the high purity of Ni-Cu_2O HNWs prepared by this simple solution process. The relatively intense (111) peak, compared to others, of Cu_2O in HNWs would facilitate the photodegradation.[40,51-53] In addition, there is no obvious shift of all Ni diffraction peaks in composites, implying that Cu_2O NPs only bind on the surfaces without distorting the lattice of Ni NWs. All the results demonstrate the successful formation of Ni-Cu_2O HNWs by the present method.

The UV-Vis-NIR absorption spectra of Ni NWs, Cu_2O NPs, and Ni-Cu_2O HNWs in ethanol are presented in Fig. 5e. The spectrum of pure Ni NWs shows featureless and monotonously decreases in absorbance with the increase in wavelength, whereas the pure Cu_2O NPs shows a characteristic absorption peak at 458 nm, which is slightly red-shifted to 464 nm in Ni-Cu_2O composites due to parts of the surface of Cu_2O contact with Ni NWs which possess higher refractive index than ethanol. Comparing with pure Cu_2O NPs, the absorbance of Ni-Cu_2O composites is broadened from UV window to near-infrared and covers almost all the UV−Visible light spectra, which avails to take full advantage of the sunlight.

It should be noted that the solvent can make a remarkable effect on the formation of Ni-Cu_2O HNWs. As shown in Figure 6a-c, more Cu_2O NPs were formed by using solvents with lower polarity. The decrease of polarity from methanol to propanol may compel more Cu^{2+} to adsorb on the surface of Ni NWs modified by PVP rather than disperse in the solvent, leading sufficient amount of Cu^{2+} to grow into $Cu(OH)_2$ around the pricks of Ni NWs after adding $N_2H_4 \cdot H_2O$. Synthetically considering the photocatalytic efficiency, preparation cost and environmental protection, 1D Ni Cu_2O HNWs prepared in ethanol was selected to photodegrade MO under irradiation.

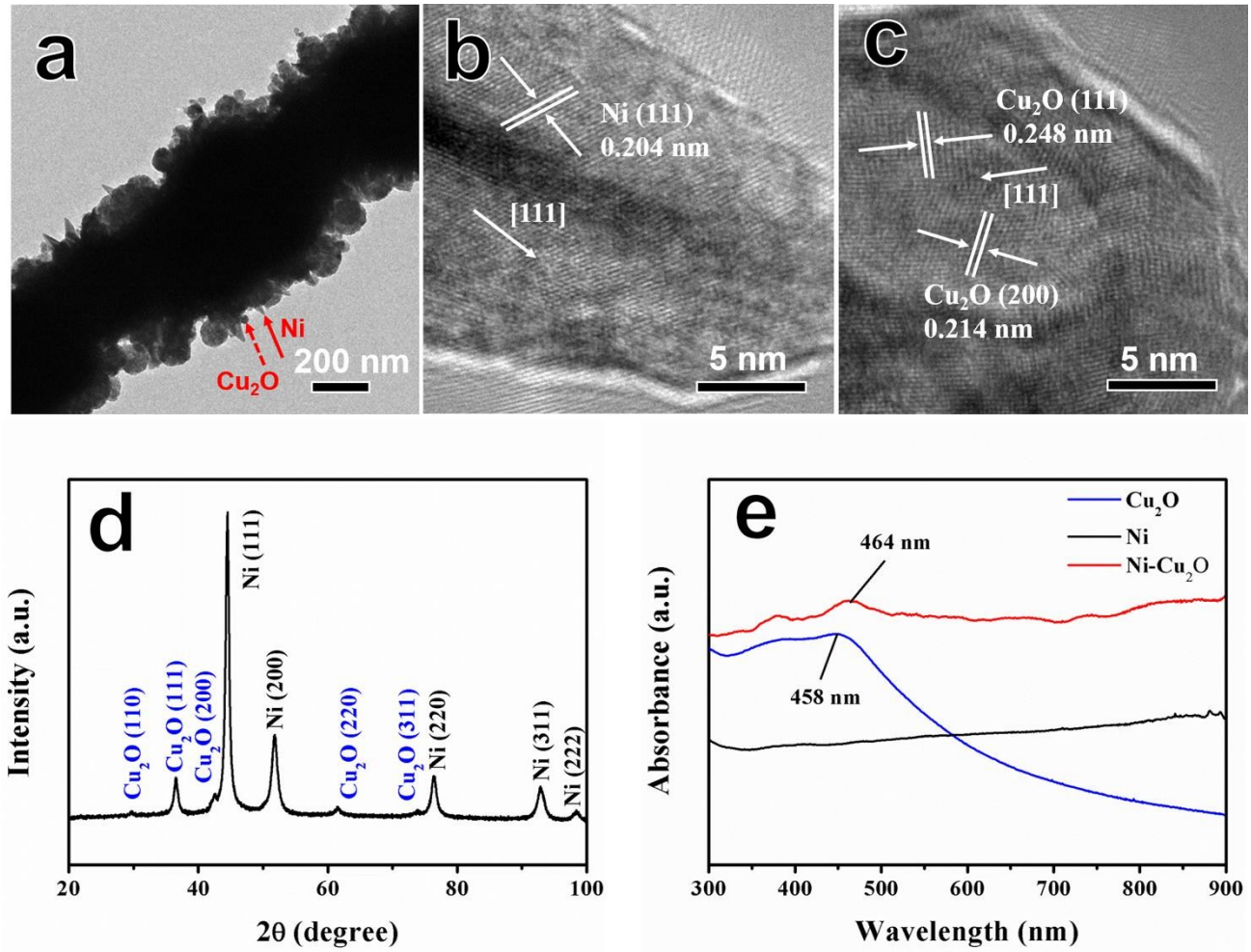

Fig. 5. (a) TEM image, (b) and (c) HRTEM images (taken from the red arrows region in Fig. 5a), and (d) XRD pattern of Ni-Cu_2O HNWs, and (e) UV−vis absorption spectra of as-prepared photocatalysts in ethanol.

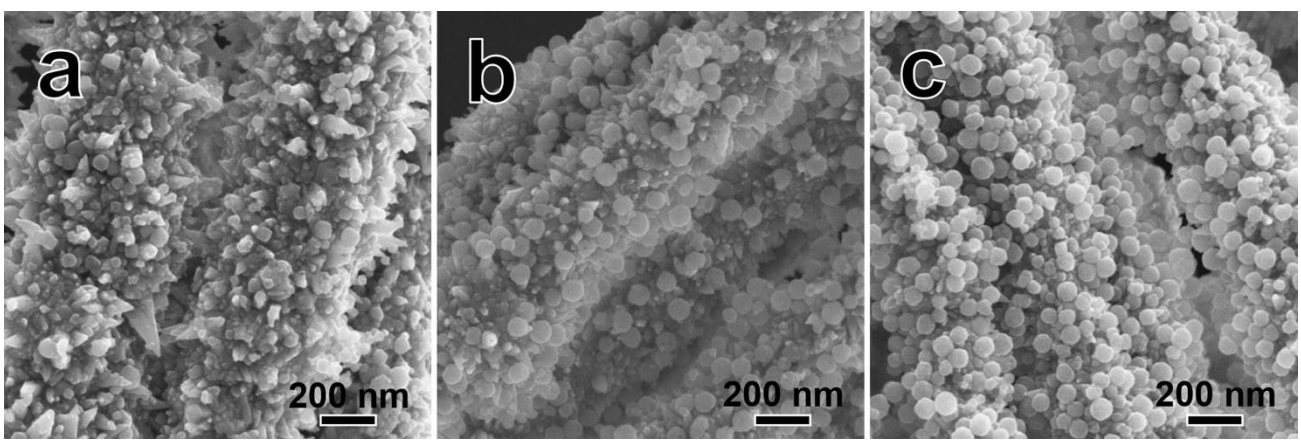

Fig. 6 SEM image of Ni-Cu_2O HNWs prepared in different solvents: (a) methanol, (b) ethanol, and (c) propanol.

Pure Cu_2O NPs were also prepared by this method without adding Ni NWs. Fig. 7a shows that the spherical Cu_2O NPs have a rough surface with the sizes ranging from 20 nm to 140 nm (as shown in Fig. S3). The corresponding XRD pattern of pure Cu_2O

NPs in Fig. 7b exhibits five strong diffraction peaks which can be indexed to Cu_2O (JCPDS 5−667) and consistent with the result of Cu_2O in the composites (Fig. 5d), meaning the pure Cu_2O NPs with a yellow colour also can be synthesized by this method (inset in Fig. 7b). The EDX measurements were performed to characterize the chemical composition of pure Cu_2O, and the result clearly shows the presence of Cu and O (Fig. S4).

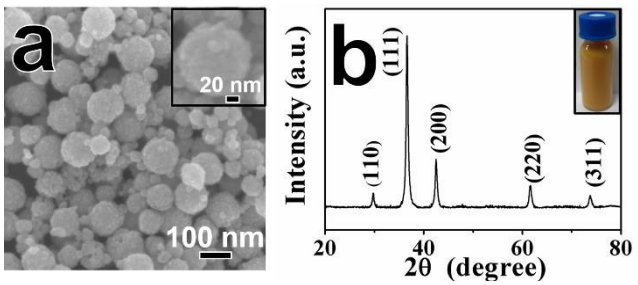

Fig. 7 (a) SEM image and (b) XRD pattern of pure Cu_2O NPs. The insert in (a) and inset in (b) are magnified SEM and solution of pure Cu_2O NPs, respectively.

Fig. 8a shows the comparison of photocatalytic activity of Ni NWs, Cu_2O NPs and Ni-Cu_2O HNWs, respectively. It can be clearly observed that pure Ni NWs exhibits no photocatalytic ability for the degradation of MO, while both Ni-Cu_2O HNWs and Cu_2O NPs show highly photocatalytic activities. When using pure Cu_2O NPs as catalyst, the photodegradation rate of MO is 72% during 80 min, however, which up to 94% by using Ni-Cu_2O HNWs (the photodegradation processes shown in Fig. S5). From Fig. 8b, it can be concluded that, although, Ni-Cu_2O HNWs and Cu_2O NWs have similar adsorption ratios due to the approximative weight of Cu_2O (the adsorption processes shown in Fig. S6), the degradation rates of these two materials are significantly different. Fig. 8a clearly manifests that Ni NWs can neither adsorb nor photodegrade MO, thus, the improvement in photodegradation of MO should ascribe to the synergistic effect of Cu_2O NPs and Ni NWs in the heteronanowires. The apparent rate constant k value is 0.03417 and 0.0157 min^{-1} for Ni-Cu_2O HNWs and Cu_2O NPs, respectively. Compared with previously reports, our Ni-Cu_2O HNWs are superior to Cu-Cu_2O polyhedron[50] and Cu_2O-Au NPs[30] in degradation of MO. As shown in Table 1, although the performance of catalysts could not be fairly estimated due to the different photocatalytic condition, such as the concentration of MO, additive amount of catalysts, irradiation time and light source, it can be still concluded that nickel is an alternative candidate for substituting the noble metal to improve the photocatalytic ability of Cu_2O.

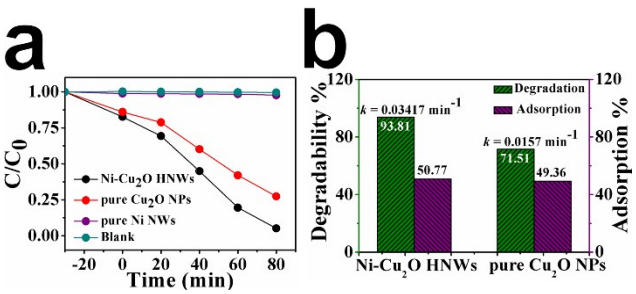

Fig. 8 (a) Photodegradation of MO by different catalysts under irradiation for 80 min, and (b) photodegradation rate (green) under irradiation and adsorption rate (violet) in the dark of Ni-Cu_2O HNWs and pure Cu_2O NPs.

The stability of the as-prepared photocatalyst was assessed by the recycling performance on degradation of MO. Fig. 9 indicates that the degradation ratio is decreased after several cycles. Approximately 44% of photocatalytic activity is lost in the third cycle, which mainly ascribed to the inevitable weight loss during the recycle, as shown in Fig. 9a. Moreover, during the irradiation, Cu_2O is photo-oxidized into CuO by accumulated holes in the VB, which is a poor photocatalyst due to serious recombination and weak redox ability of those excited e^- and h^+ compared with Cu_2O.[44,54] This amorphous CuO NPs could not be detected through XRD measurement.[55]

Strikingly, the morphologies of as-prepared photocatalysts change after photocatalytic process, and more sheet-like structures are formed as the photocatalytic time increased (Fig. S7). However, XRD patterns of Ni-Cu_2O HNWs before and after photocatalytic process show unobvious changes except the weakened intensity of Cu_2O peaks (Fig. S8). In addition, the density of Cu_2O NPs in heteronanowires decreases, and the surfaces become rougher, which may significantly affect the photocatalytic efficiency. All these morphology transformations are similar to the previous reports.[28,52,56]

Table 1. Comparison of degradability for different metal-Cu_2O heterostructures photocatalyst

Photocatalyst	Additive Amount (mg)	MO (mg/ L)	Degradation (%)	Irradiation time (min)	Light source	Ref.
Ni-Cu_2O HNWs	20	20	94	80	300 W Xe lamp ($\lambda > 420$ nm)	This work
Nanoporous Cu@Cu_2O	4	20	90	100	Sun light (300–2500 nm)	31
Hollow Cu@Cu_2O	10	100	92	30	500 W Xe lamp ($\lambda > 400$ nm)	44
Cu-Cu_2O polyhedron	150	10	~80	90	500 W Xe lamp ($\lambda \geq 400$ nm)	50
Cu_2O@Cu NPs	30	10	90	120	40 W tungsten lamp (350–2500 nm)	55
Ag@Cu_2O HNWs	5	NA [a]	92	140	LSC-100Solar Simulator	28
Ag@Cu_2O NPs	NA [a]	15	~75	120	8 W visible lamp (400–700 nm)	27
Cu_2O-Au NPs	20	400	~60	240	500 W Xe arc lamp ($\lambda > 420$ nm)	30
Au@Cu_2O octahedra	10.6	13	91	40	500 W Xe lamp ($\lambda > 400$ nm)	41

[a]NA, not available.

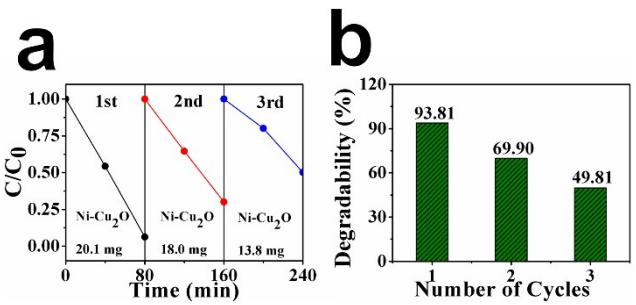

Fig. 9 (a) Degradability of different cycles for photodegradation of MO in the presence of Ni-Cu_2O HNWs, and (b) photocatalytic degradation rate at different recycling times.

The ability of Ni-Cu_2O HNWs to photodegrade other organic dyes was also examined, as shown in Fig. S9. The apparent rate constant k value is 0.00952 and 0.00612 min^{-1} for OG and RhB, respectively. Both OG and RhB can be photodegraded by Ni/Cu_2O HWNs at a slow rate. The catalytic efficiency is different for the three dyes (MO, OG and RhB) which may be influenced by the molecular size and structure, as well as the electrical nature of dyes.[57]

It has been reported that the metal/semiconductor heteroarchitecture can accelerate the charge transfer and suppress the recombination of photo-induced e^--h^+ pairs.[10,11,22,31] A possible mechanism is proposed to explain the enhanced photocatalytic activity of 1D Ni-Cu_2O HNWs on the photodegradation of MO as illustrated in Fig. 10. When irradiated by light, the e^- in VB of Cu_2O can be excited to the conduction band (CB) in Ni-Cu_2O HNWs, and then rapidly transfer to Ni NWs, which effectively prevents the recombination of the photogenerated e^--h^+ pairs and facilitates the charge separation at the interface, improving the photocatalytic ability (eqn (4)). The accumulated e^- in Ni NWs and h^+ in the VB of Cu_2O can react with H_2O or O_2 which adsorbed on the surface of the catalyst to produce reactive species, such as superoxide radical anions ($\bullet O^{2-}$) and hydroxyl radical ($\bullet$OH) which play key roles in the photocatalysis process (eqn (5-9)). The hydroxyl radical $\bullet$OH can oxidize the adsorbed MO with a high efficiency due to the higher redox potential (+1.9 V) than that of MO (+0.94 V).

$$Cu_2O/Ni + h\nu \xrightarrow{\lambda > 420\ nm} Cu_2O(h^+)/Ni(e^-) \quad (4)$$

$$e^- + O_2 \rightarrow \cdot O_2^- \quad (5)$$

$$\cdot O_2^- + H_2O \rightarrow H_2O_2 + \cdot OH \quad (6)$$

$$H_2O_2 + e^- \rightarrow \cdot OH + OH^- \quad (7)$$

$$h^+ + H_2O \rightarrow H + \cdot OH \quad (8)$$

$$\cdot O_2^-/\cdot OH + \text{organic dye} \rightarrow CO_2 + H_2O \quad (9)$$

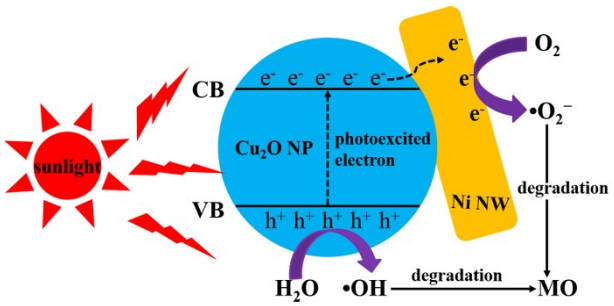

Fig. 10 Schematic illustration of the transfer of photogenerated e^--h^+ pairs in the Ni-Cu_2O HNWs under light irradiation

Based on the proposed photocatalytic mechanism, Ni NWs in this heterostructures act as an electron sink to capture the photoexcited e^- from the semiconductor Cu_2O, deferring the recombination of e^--h^+ pairs. It is well known that fluorescence emission is related to the recombination of e^--h^+ pairs, and the weak intensity of fluorescence signifies the low recombination rate. [25,34,58] As shown in Fig. 11a, the introduction of Ni NWs diminishes emission intensity of the fluorescence spectrum due to energy or charge transfer from Cu_2O NPs to the Ni nanowires, indicating that the recombination rate of photo-induced e^--h^+ pairs is effectively reduced, thus leading to an increased charge carrier separation. Additionally, the unique 1D Ni nanowires in heteroarchitecture with excellent electron conductivity and mobility induce the fast and long-distance electron transport and also provide adsorb sites for MO (the BET surface area of Ni-Cu_2O is 7.62 m^2g^{-1}, Fig. S10) .The EIS were used to investigate more details about the charge transport in the composites. The semicircular arc of Ni-Cu_2O HNWs is smaller than that of pure Cu_2O NPs in Fig. 11b, indicating a decrease of the solid state interface layer resistance and the charge transfer resistance on the surface. It is suggested that Ni NWs can serve as an effective e^- acceptor to inhibit the direct recombination of photoexcited e^--h^+ pairs in Cu_2O and thus enhance the photocatalytic activity.[44,59] Overall, in these two competitive systems, the charge transfer process can surpass the recombination process mainly due to both electron-accepting and transporting properties of Ni NWs in the composites.

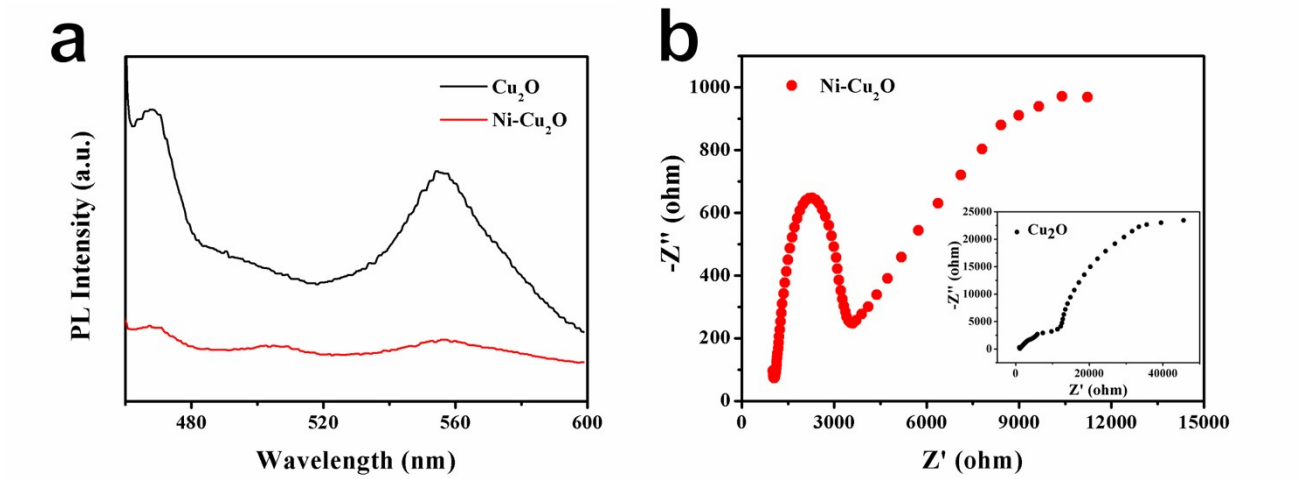

Fig. 11. (a) Fluorescence spectra of Cu_2O NPs and Ni-Cu_2O HNWs with the excitation wavelength of 440 nm, and (b) the electrochemical impedance spectroscopy: Nyquist plot of Ni-Cu_2O HNWs and Cu_2O NPs (inset).

4 Conclusions

In summary, low-cost and magnetic 1D Ni-Cu_2O HNWs with efficient photodegradation activity have been fabricated by a facile method. The improvement of the photocatalytic activity on the photodegradation of MO is due to the enhanced light absorption, unique 1D nanostructure and electron sink effect of Ni NWs in the heteronanowires. It is believed that such rational design is suitable for the fabrication of Cu_2O-based metal-semiconductor heterostructures, and such recyclable 1D photocatalyst may hold great potential in the application of photocatalysis.

Acknowledgements

This work was supported by National High Technology Research and Development Program of China (No. 2011AA050504), National Natural Science Foundation of China (21171117), Shanghai Natural Science Foundation (No. 13ZR1456600), National Natural Science Foundation of China (No.51272155), and the Program for Professor of Special Appointment (Eastern Scholar) at Shanghai Institutions of Higher Learning. We also acknowledge support from the Instrumental Analysis Center of Shanghai Jiao Tong University and the Center for Advanced Electronic Materials and Devices of Shanghai Jiao Tong University.

Notes and references

Key Laboratory for Thin Film and Microfabrication of Ministry of Education, Department of Micro/Nano Electronics, School of Electronic Information and Electrical Engineering, Shanghai Jiao Tong University, Shanghai 200240, P. R. China. E-mail: zhiyang@sjtu.edu.cn; yfzhang@sjtu.edu.cn; Tel.:+86-21-34206398; Fax: +86-34205665

Electronic Supplementary Information (ESI) available: The size distribution of Cu_2O in heteronanowires; the EDX spectra of as-synthesized Ni-Cu_2O HNWs; the size distribution of pure Cu_2O; the EDX spectra of pure Cu_2O NPs; variation in the absorption of the MO solution in the presence of the as-prepared photocatalysts for different irradiation times; XRD patterns and SEM images of Ni-Cu_2O before and after photocatalytic test; the adsorption curves of MO in the presence of the as-prepared photocatalysts under dark for different times; the ICP results of Ni-Cu_2O HNWs.See DOI: 10.1039/b000000x/

1 N.Q. Wu, J. Wang, D. Tafen, H. Wang, J. G. Zheng, J. P. Lewis, X.G. Liu, S. S. Leonard, A. Manivannan, *J. Am. Chem. Soc.*, 2010, **132**, 6679.

2 Z. Liu, X. Zhang, S. Nishimoto, T. Murakami, A. Fujishima, *Environ. Sci. Technol*., 2008, **42**, 8547.

3 H. G. Yang, C. H. Sun, S. Z. Qiao, J. Zou, G. Liu, S. C. Smith, H. M. Cheng, G. Q. Lu, *Nature*, 2008, **453**, 638.

4 A. McLaren, T. Valdes-Solis, G. Li, S. C. Tsang, *J. Am. Chem. Soc.*, 2009, **131**, 12540.

5 H. Bao, W. Zhang, D. Shang, Q. Hua, Y. Ma, Z. Jiang, J. Yang, W. Huang, *J. Phys. Chem. C*, 2010, **114**, 6676.

6 C. H. Kuo, M. H. Huang, *Nano Today*, 2010, **5**, 106.

7 H. P. Liu, T. Ye and C. D. Mao, *Angew. Chem. Int. Ed.*, 2007, **46**, 6473–6475. C. Tian, Q. Zhang, A. Wu, M. Jiang, Z. Liang, B. Jiang, H. Fu, *Chem. Commun.*, 2012, **48**, 2858.

8 Y. Zhao, W. Wang, Y. Li, Y. Zhang, Z. Yan, Z. Huo, *Nanoscale*, 2014, **6**, 195.

9 P. Wang, B. Huang, Y. Dai, M. H. Whangbo, *Phys. Chem. Chem. Phys.*, 2012, **14**, 9813.

10 N. Zhang, S. Liu, Y. J. Xu, *Nanoscale*, 2012, **4**, 2227.

11 W. Hou, S. B. Cronin, *Adv. Funct. Mater*., 2013, **23**, 1612.

12 Y. Qu, X. Duan, *Chem. Soc. Rev.*, 2013, **42**, 2568.

13. R. Jiang, B. Li, C. Fang, J. Wang, *Adv. Mater.*, 2014, **26**, 5274.

14 L. P. Zhu, N. C. Bing, D. D. Yang, Y. Yang, G. H. Liao, L. J. Wang, *CrystEngComm*, 2011, **13**, 4486.

15 M. Deo, D. Shinde, A. Yengantiwar, J. Jog, B. Hannoyer, X. Sauvage, M. More, S. Ogale, *J. Mater. Chem.*, 2012, **22**, 17055.

16 F. Mou, L. Xu, H. Ma, J. Guan, D. R. Chen, S. Wang, *Nanoscale*, 2012, **4**, 4650.

17 W. Wu, S. Zhang, X. Xiao, J. Zhou, F. Ren, L. Sun, C. Jiang, *ACS Appl. Mater. Interfaces*, 2012, **4**, 3602.

18 M. Wang, L. Sun, Z. Lin, J. Cai, K. Xie, C. Lin, *Environ. Sci. Technol.*, 2013, **6**, 1211.

19 Y. Wang, K. Yu, H. Yin, C. Song, Z. Zhang, S. Li, H. Shi, Q. Zhang, B. Zhao, Y. Zhang, Z. Zhu, *J. Phys. D: Appl. Phys.*, 2013, **46**, 175303.

20 Q. Tian, W. Wu, L. Sun, S. Yang, M. Lei, J. Zhou, Y. Liu, X. Xiao, F. Ren, C. Jiang, V. A. Roy, *ACS Appl. Mater. Interfaces*, 2014, **6**, 13088.

21 T. Hirakaw, P. V. Kamat, *J. Am. Chem. Soc.*, 2005, **127**, 3928.

22 R. Georgekutty, M. K. Seery, S. C. Pillai, *J. Phys. Chem. C*, 2008, **112**, 13563.

23 Y. Zheng, C. Chen, Y. Zhan, X. Lin, Q. Zheng, K. Wei, J. Zhu, *J. Phys. Chem. C*, 2008, **112**, 10773.

24 Z. Wang, S. Zhao, S. Zhu, Y. Sun, M. Fang, *CrystEngComm*, 2011, **13**, 2262.

25 Y. Pan, S. Deng, L. Polavarapu, N. Gao, P. Yuan, C. H. Sow, Q. H. Xu, *Langmuir*, 2012, **28**, 12304.

26 F. Xiao, *J. Phys. Chem. C*, 2012, **116**, 16487.

27 J. Li, S. K. Cushing, J. Bright, F. Meng, T. R. Senty, P. Zheng, A. D. Bristow, N. Wu, *ACS Catal.*, 2013, **3**, 47.

28 J. Xiong, Z. Li, J. Chen, S. Zhang, L. Wang, S. Dou, *ACS Appl. Mater. Interfaces*, 2014, **6**, 15716.

29 L. Xu, L. P. Jiang, J. J. Zhu, *Nanotechnology*, 2009, **20**, 045605.

30 Q. L. Wang, H. Z. Zheng, Y. J. Long, L. Y. Zhang, M. Gao and W. J. Bai, Carbon, 2011, **49**, 3134–3140. Q. Hua, F. Shi, K. Chen, S. Chang, Y. Ma, Z. Jiang, G. Pan, W. Huang, *Nano Res.*, 2011, **4**, 948.

31 T. Kou, C. Jin, C. Zhang, J. Sun, Z. Zhang, *RSC Adv*., 2012, **2**, 12636.

32 S. Sun, H. Liu, L. Wu, C. E. Png, P. Bai, *ACS Catal.*, 2014, **4**, 4269.

33 D. Barreca, P. Fornasiero, A. Gasparotto, V. Gombac, C. Maccato, T. Montini, E. Tondello, *ChemSusChem*, 2009, **2**, 230.

34 X. Meng, D. Geng, J. Liu, R. Li, X. Sun, *Nanotechnology*, 2011, **22**, 165602.

35 L. Zhang, D. A. Blom, H. Wang, *Chem. Mater.*, 2011, **23**, 4587.

36 W. Zhao, W. Fu, H. Yang, C. Tian, M. Li, Y. Li, L. Zhang, Y. Sui, X. Zhou, H. Chen, G. Zou, *CrystEngComm*, 2011, **13**, 2871.

37 L. Zhang, H. Jing, G. Boisvert, J. Z. He, H. Wang, *ACS nano*, 2012, **6**, 3514.

38 S. M. Majhi, P. Rai, S. Raj, B. S. Chon, K. K. Park, Y. T. Yu, *ACS Appl. Mater. Interfaces*, 2014, **6**, 7491.

39 P. Rai, R. Khan, S. Raj, S. M. Majhi, K. K. Park, Y. T. Yu, I. H. Lee, P. K. Sekhar, *Nanoscale*, 2014, **6**, 581.

40 C. H. Kuo, Y. C. Yang, S. Gwo, M. H. Huang, *J. Am. Chem. Soc.*, 2011, **133**, 1052.

41 L. Kong, W. Chen, D. Ma, Y. Yang, S. Liu, S. Huang, *J. Mater. Chem.*, 2012, **22**, 719.

42 Z. Ai, L. Zhang, S. Lee, W. Ho, *J. Phys. Chem. C*, 2009, **113**, 20896.

43 L. Xu, C. Srinivasakannan, J. Peng, M. Yan, D. Zhang, L. Zhang, *Appl. Surf. Sci.*, 2015, **331**, 449.

44 X. Zou, H. Fan, Y. Tian, M. Zhang, X. Yan, *Dalton Trans.*, 2015, **44**, 7811.

45 S. H. Zhang, S. L. Gai, F. He, Y. L. Dai, P. Gao, L. Li, Y. J. Chen, P. P. Yang, *Nanoscale*, 2014, **6**, 7025.

46 K. Bhowmik, A. Mukherjee, M. K. Mishra, G. De, *Langmuir*, 2014, **30**, 3209.

47 Y. L. Guo, D. Wang, X. Y. Liu, X. D. Wang, W. S. Liu, W. W. Qin, *New J. Chem.*, 2014, **38**, 5861.

48 S. S. Xu, X. L. Li, Z. Yang, T. Wang, M. H. Xu, L. L. Zhang, C. Yang, N. T. Hu, D. N. He, Y. F. Zhang, *Electrochim. Acta*, 2015, **182**, 464.

49 J. Wang, L. Wei, L. Zhang, C. Jiang, E. Siu-Wai Kon, Y. Zhang, *J. Mater. Chem.*, 2012, **22**, 8327.

50 S. Sun, C. Kong, H. You, X. Song, B. Ding, Z. Yang, *CrystEngComm*, 2012, **14**, 40.

51 J. Y. Ho, M. H. Huang, *J. Phys. Chem. C*, 2009, **113**, 14159.

52 Z.K. Zheng, B. B. Huang, Z.Y. Wang, M. Guo, X.Y. Qin, X.Y. Zhang, P. Wang, Y. Da, *J. Phys. Chem. C*, 2009, **113**, 14448.

53 W. C. Wang, L. M. Lyu, M. H. Huang, *Chem. Mater.*, 2011, **23**, 2677.

54 L. Huang, F. Peng, H. Yu, H. Wang, *Solid State Sci.*, 2009, **11**, 129.

55 B. Zhou, Z. Liu, H. Wang, Y. Yang, W. Su, *Catal. Lett.*, 2009, **132**, 75.

56 L. Pan, J. J. Zou, T. Zhang, S. Wang, Z. Li, L. Wang, X. Zhang, *J. Phys. Chem. C*, 2014, **118**, 16335.

57 J. Hu, Y. L. Dong, Z. Rahman, Y. H. Ma, C. L. Ren, X. G. Chen, *Chem. Eng. J.*,2014, **254**,514.

58 Y. Ito, K. Matsuda, Y. Kanemitsu, *Phys. Rev. B*, 2007, **75**, 033309.

59 Q. P. Luo, X. Y. Yu, B. X. Lei, H. Y. Chen, D. B. Kuang, C. Y. Su, *J. Phys. Chem. C*, 2012, **116**, 8111.

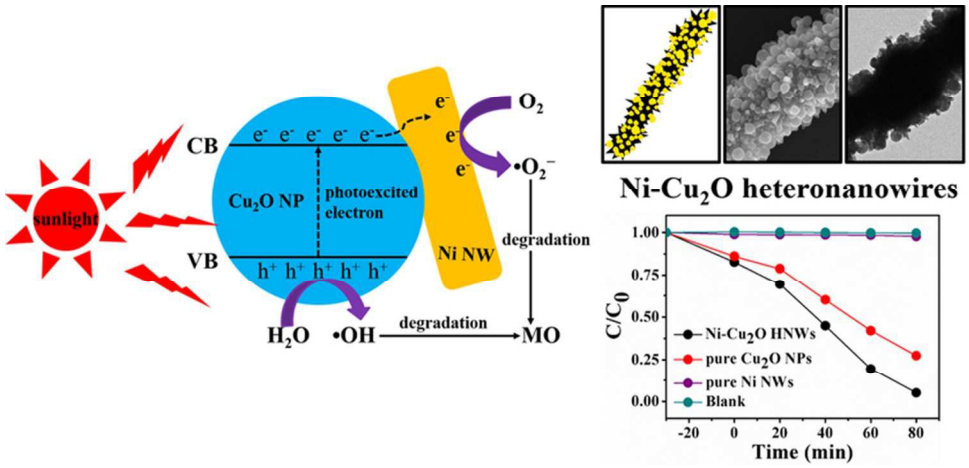

36x16mm (600 x 600 DPI)